
This item was submitted to [Loughborough's Research Repository](#) by the author.
Items in Figshare are protected by copyright, with all rights reserved, unless otherwise indicated.

Ionospheric phase scintillation index estimation based on 1 Hz geodetic GNSS receiver measurements by using continuous wavelet transform

PLEASE CITE THE PUBLISHED VERSION

<https://doi.org/10.1029/2021SW003015>

PUBLISHER

American Geophysical Union

VERSION

VoR (Version of Record)

PUBLISHER STATEMENT

This is an Open Access Article. It is published by American Geophysical Union under the Creative Commons Attribution-NonCommercial-NoDerivatives 4.0 International Licence (CC BY-NC-ND). Full details of this licence are available at: <https://creativecommons.org/licenses/by-nc-nd/4.0/>




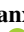
LICENCE

CC BY-NC-ND 4.0

REPOSITORY RECORD

Zhao, Dongsheng, Wang Li, Chendong Li, Xu Tang, Qianxin Wang, Craig Hancock, Gethin Wyn Roberts, and Kefei Zhang. 2022. "Ionospheric Phase Scintillation Index Estimation Based on 1 Hz Geodetic GNSS Receiver Measurements by Using Continuous Wavelet Transform". Loughborough University. <https://hdl.handle.net/2134/21647888.v1>.

Ionospheric Phase Scintillation Index Estimation Based on 1 Hz Geodetic GNSS Receiver Measurements by Using Continuous Wavelet Transform

Dongsheng Zhao^{1,2} , Wang Li^{1,2} , Chendong Li³, Xu Tang⁴, Qianxin Wang^{1,2}, Craig M. Hancock⁵, Gethin Wyn Roberts^{6,7} , and Kefei Zhang^{1,2} 

¹Key Laboratory of Land Environment and Disaster Monitoring, Ministry of Natural Resources, China University of Mining and Technology, Xuzhou, China, ²School of Environment and Spatial Informatics, China University of Mining and Technology, Xuzhou, China, ³Faculty of Science and Engineering, University of Nottingham Ningbo China, Ningbo, China, ⁴School of Remote Sensing and Geomatics Engineering, Nanjing University of Information Science and Technology, Nanjing, China, ⁵School of Architecture Building and Civil Engineering, Loughborough University, Loughborough, UK, ⁶Department of Land and Sea Mapping, Faroese Environment Agency, Tórshavn, Faroe Islands, ⁷Faculty of Natural Sciences and Technology, University of the Faroe Islands, Tórshavn, Faroe Islands

Key Points:

- A new method is proposed to extract the scintillation index by applying cycle slip detection, geodetic detrending and wavelet transform
- The scintillation index can be extracted from each carrier of the 1s-sampling-interval Global Navigation Satellite System observations
- The extracted scintillation index can provide a consistent performance in monitoring scintillation as that given by Ionospheric Scintillation Monitoring Receiver

Correspondence to:

K. Zhang and W. Li,
profkzhang@cumt.edu.cn;
liwang@cumt.edu.cn

Citation:

Zhao, D., Li, W., Li, C., Tang, X., Wang, Q., Hancock, C. M., et al. (2022). Ionospheric phase scintillation index estimation based on 1 Hz geodetic GNSS receiver measurements by using continuous wavelet transform. *Space Weather*, 20, e2021SW003015. <https://doi.org/10.1029/2021SW003015>

Received 16 DEC 2021

Accepted 13 APR 2022

Author Contributions:

Data curation: Dongsheng Zhao, Qianxin Wang

Formal analysis: Dongsheng Zhao

Funding acquisition: Kefei Zhang

Investigation: Dongsheng Zhao, Chendong Li

Methodology: Dongsheng Zhao, Wang Li

Resources: Dongsheng Zhao

Software: Dongsheng Zhao

Supervision: Craig M. Hancock, Gethin Wyn Roberts, Kefei Zhang

Validation: Dongsheng Zhao, Wang Li, Xu Tang

Abstract The adverse effect of the ionospheric scintillation on Global Navigation Satellite System (GNSS) requires scintillation monitoring on a global scale. Ionospheric Scintillation Monitoring Receivers (ISMR) are usually adopted to monitor scintillation, while they are not suitable for global monitoring due to the 50 Hz data collecting rate, which restricts the distribution. This paper proposes a new method to extract the phase scintillation index from each GNSS carrier with 1s-sampling-interval, mainly based on the cycle slip detection, the geodetic detrending and the wavelet transform, in which the optimal symmetry parameter and the time-bandwidth product are determined with trial calculation. Taken the σ_ϕ index provided by ISMR as the reference, 1-year observations are utilized to evaluate the scintillation monitoring performance of the extracted index regarding the correlation of the magnitude in each observation arc, the detected daily scintillation occurrence rate, the diurnal variation pattern of the ionospheric scintillation, the correlation between the scintillation occurrence rate and the space weather parameter, and the complementary cumulative distribution of the magnitudes. Compared to the performance of Rate of Total electron content Index, a higher consistency can be achieved between the extracted index and the σ_ϕ index, indicating the rationality of applying the proposed method in monitoring scintillations. The extracted scintillation index can be expected to introduce geodetic receivers operating at 1s-sampling-interval into the field of ionospheric scintillation monitoring on a global scale.

Plain Language Summary Small scale structures in the ionosphere will interfere with the amplitude and phase of the Global Navigation Satellite System (GNSS) signals passing through them. This phenomenon is called ionospheric scintillation, which can affect the positioning navigation and timing services of GNSS, calling for the need of monitoring ionospheric scintillations on a global scale. A special type of receiver, called Ionospheric Scintillation Monitoring Receiver (ISMR), is usually needed in ionosphere monitoring. However, due to the high sampling rate and price, the distribution of ISMR is limited, making it impossible to realize large-scale ionospheric scintillation monitoring using only ISMR. In order to solve this problem, this paper proposes a new method to extract the scintillation index from the widely distributed geodetic receivers. Although the existing Rate of Total electron content Index (ROTI) can also use geodetic receivers for ionospheric scintillation monitoring, experiments based on long-period observations collected in the Arctic region of the North America show that the extracted scintillation index can be more accurate than ROTI and the scintillation information on each carrier can be provided. The extracted scintillation index provides a basis for realizing global ionospheric scintillation monitoring and modeling in the future.

1. Introduction

The electromagnetic wave signal passing through ionospheric irregularities produces rapid fluctuations in amplitude or phase, which is called ionospheric scintillation. This phenomenon can reduce the carrier-to-noise ratio and even cause loss-of-lock of the Global Navigation Satellite System (GNSS) signals, thereby interfering with GNSS positioning navigation and timing services. It calls for an urgent need in studying and effectively monitoring the

© 2022. The Authors.

This is an open access article under the terms of the [Creative Commons Attribution-NonCommercial-NoDerivs License](https://creativecommons.org/licenses/by/4.0/), which permits use and distribution in any medium, provided the original work is properly cited, the use is non-commercial and no modifications or adaptations are made.

Writing – original draft: Dongsheng Zhao
Writing – review & editing: Dongsheng Zhao, Wang Li, Chendong Li, Xu Tang, Qianxin Wang, Craig M. Hancock, Gethin Wyn Roberts, Kefei Zhang

ionospheric scintillation to overcome its adverse impact. Due to the continuous and extensive characteristics of GNSS observations, GNSS has become an important source of information for ionospheric scintillation monitoring. Ionospheric scintillation index, measured from GNSS observations, is a quantitative characterization of the strength of ionospheric scintillation, and is the foundation for realizing ionospheric scintillation monitoring and forecasting. Therefore, the investigation on extracting the ionospheric scintillation index more accurately is of great significance for scientific understanding about the occurrence of ionospheric scintillation, thereby reducing the adverse effect of ionospheric scintillation (Guo et al., 2021; Xu et al., 2020).

One of the main equipment on monitoring scintillations is the ionospheric scintillation monitoring receiver (ISMR), which can provide two types of indices: the amplitude scintillation index (S_4) and the phase scintillation index (σ_ϕ). Due to the differences in the generation mechanism of ionospheric scintillation in the low latitude and the polar regions (Luan et al., 2015; Mitchell et al., 2005), amplitude scintillations often occur in the low latitude region, while phase scintillations dominate in the polar region (Zhao, Li, Wang, et al., 2022). To reflect the variation information of the scintillation in the Arctic region, which is the interest area of this research, the phase scintillation index will be extensively studied in this paper. The phase scintillation index provided by ISMR, namely σ_ϕ , can be calculated as follows,

$$\sigma_\phi = \sqrt{\langle \phi^2 \rangle - \langle \phi \rangle^2} \quad (1)$$

where ϕ represents the carrier phase measurement detrended by a sixth-order Butterworth filter with 0.1 Hz cutoff frequency (Van Dierendonck et al., 1993); $\langle \cdot \rangle$ denotes the expectation within a certain time interval, which is usually set to 60s. The magnitude of σ_ϕ indicating the occurrence of the scintillation is a controversial value. This paper selects 0.2 rad as the threshold to determine the occurrence of scintillations on the GPS L1 signal according to our experiences and the existing studies (e.g., Jiao et al., 2013; Linty et al., 2018), while the magnitudes below the 0.2 rad might also be caused by weak scintillations, although they are usually hard to distinguish from the measurement noise.

A high-price receiver clock is equipped in an ISMR to capture the phase fluctuations caused by scintillations. Besides, substantial memories are needed to support the 50 Hz data collection. The high price and substantial memories limit the density of ISMR networks. Currently, the ionospheric scintillation monitoring networks mainly include Monitor (European Union) (Béniguel et al., 2017), CIGALA/CALIBRA (Brazil) (Vani et al., 2017) and Canadian High Arctic Ionospheric Network (CHAIN) (Canada) (Jayachandran et al., 2009), deployed with a total of about 150 ISMRs, of which only 31 stations are located in the Arctic region. Therefore, it is difficult to monitor ionospheric scintillations in a large area, for example, the Arctic region, using only the ISMR scintillation index.

Compared with ISMR, geodetic receivers are less expensive and more widely distributed. The extraction of the ionospheric scintillation index based on geodetic receivers benefits the monitoring study on the ionospheric scintillation in the Arctic region. Geodetic receivers usually collect observations at low sampling interval (no larger than 1s), which makes it difficult to measure the ionospheric scintillation from carrier phase measurements accurately using only high-pass filtering methods, calling for the need of eliminating the influence of other error sources. Taking advantage of the dual- or triple-frequency signals, multi error sources can be eliminated by the combined signals. For instance, Juan et al. (2018) averaged the rate of Total Electron Content (TEC) value from all the visible satellites in each epoch to generate the along arc TEC rate index, which has been selected as one of the parameters characterizing ionospheric activities by European Geostationary Navigation Overlapping Service system. In order to eliminate the influence of frequency-independent error sources, for example, multipath, Nguyen et al. (2019) and Juan et al. (2017) adopted Butterworth filters with 0.1 Hz cutoff frequency to extract ionospheric scintillation signals in the residual of the combined signals. Ahmed et al. (2015) studied the wavelet transform method to extract ionospheric scintillation signals from vertical TEC data in high latitude regions.

Of all the existing scintillation indices based on 1s-sampling-interval observations, the Rate of TEC index (ROTI) is believed to be the most widely used scintillation index (Cherniak et al., 2018; Dugassa et al., 2019; Li et al., 2018; Yang & Liu, 2016; Yizengaw & Groves, 2018). ROTI is defined as the standard deviation (STD) of the rate of TEC (Pi et al., 1997), which can be calculated as follows,

$$\text{STEC}(i) = \frac{\Phi_{L1}(i) - \Phi_{L2}(i)}{40.309 \cdot 10^{16} \cdot \left(\frac{1}{f_2^2} - \frac{1}{f_1^2} \right)} \quad (2)$$

$$\text{ROT} = \frac{\text{STEC}(i) - \text{STEC}(i - 1)}{T(i) - T(i - 1)} \quad (3)$$

$$\text{ROTI} = \sqrt{\langle \text{ROT}^2 \rangle - \langle \text{ROT} \rangle^2} \quad (4)$$

where STEC denotes the slant path TEC; Φ represents the carrier phase measurement in the unit of length; f_1 and f_2 denote the frequency of L1 and L2 signals respectively; i means the i th epoch; T stands for time in the unit of minute. ROTI has two main limitations. The first is that ROTI measures the scintillation effect in the geometry-free (GF) combination. The scintillation effects on the signals with different frequencies are not always proportional (Bhattacharyya et al., 2000; Juan et al., 2017), resulting that the scintillation on each individual frequency cannot be extracted from ROTI. The second is that ROTI is obliquity with the elevation angle (Fabbro et al., 2019), which means large ROTI values are usually obtained at low elevations. In order to fix this obliquity, a mapping function considering the satellite elevation angle is usually applied to ROTI (Nguyen et al., 2019), shown as follows,

$$M(e) = \sqrt{1 - \left(\frac{R_E}{R_E + h} \cdot \cos(e) \right)^2} \quad (5)$$

$$\text{ROTI} = \sqrt{\langle (M \cdot \text{ROT})^2 \rangle - \langle M \cdot \text{ROT} \rangle^2} \quad (6)$$

where ROTI in Equation (6) flattens the obliquity at low elevation angles; M denotes the mapping function; e is the satellite elevation angle; R_E is the radius of the Earth and h represents the height of the assumed ionospheric layer, which is set to 110 km (Prikryl et al., 2016), regarding the generation difference of the ionospheric irregularities. At the high-latitude region, irregularities can be produced by a variety of auroral and polar cap phenomena, including cusp dynamics, auroral particle precipitation, auroral blobs, and polar cap patches, which decrease the altitude of the irregularities, compared to that at the low-latitude region (Oksavik et al., 2015). ROTI is estimated from 1s-sampling-interval data over 1-min period.

This paper proposes a new method to extract the phase scintillation index from each carrier of the GNSS observations, instead of the combined signal as most of the existing methods did. The detailed procedure to conduct this method will be provided after a brief introduction to the data. Most of the existing researches validated their indices regarding the magnitude details of several observation arcs, which cannot reveal the monitoring performance of the scintillation index over a long period. Considering this drawback, this paper will evaluate the scintillation monitoring performance of the extracted scintillation index extensively with a statistical method using the observations collected in the whole year of 2020.

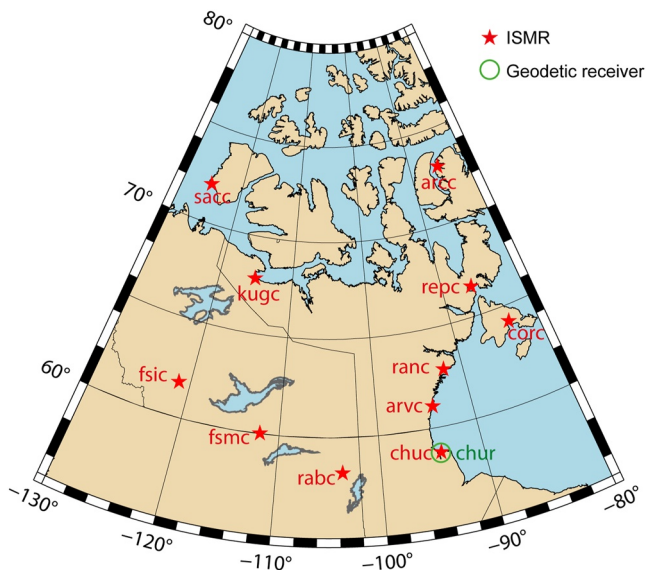


Figure 1. Distribution of the selected stations.

2. Introduction to the Adopted Data

In order to validate the accuracy of the scintillation index extracted with the proposed method in the high-latitude region, this paper selects 11 stations from CHAIN (Jayachandran et al., 2009), as shown in Figure 1. All the stations are located at either the polar cap region or the Auroral zone. Each station is equipped with one Septentrio PolaRxS Pro ionospheric scintillation monitoring receiver and a Septentrio PolaN GG antenna. All the receivers are set to collect dual-frequency GPS observations at 1/50s-sampling-interval to calculate the phase scintillation index σ_ϕ , which is taken as the reference for the validation. The observations filtered into 1s-sampling-interval are also collected to extract the scintillation index using the proposed method. This paper adopts the observations collected in the whole year of 2020, however the data during the days 1–66 of the year 2020 at the station kugc is excluded due to the reference oscillator failure.

Besides the 1s-sampling-interval data from ISMR, the GPS observations collected from the station chur, equipped with a Topcon NET-G3A geodetic

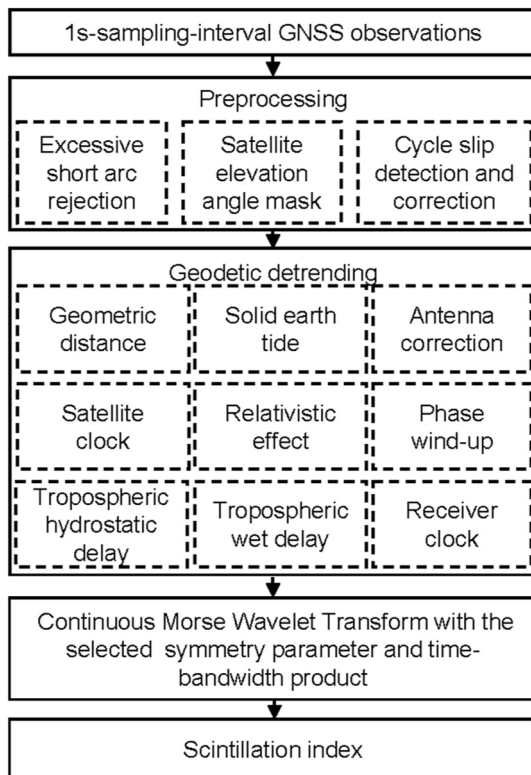


Figure 2. Procedure of extracting the phase scintillation index from 1s-sampling-interval Global Navigation Satellite System observations.

receiver, are also adopted in this paper. The station chur is part of the Canadian Active Control System and co-located with the station chuc. We collected the observations of the station chur for the whole year of 2020 at 1s-sampling-interval.

3. Method for Extracting the Phase Scintillation Index From 1s-Sampling-Interval Observations

This paper proposes a method for extracting the ionospheric phase scintillation index from each carrier of the GNSS observations with 1s-sampling-interval. After preprocessing GNSS observations, the phase scintillation index is obtained by the following two processes, including the geodetic detrending (GD) and the wavelet transform, as shown in Figure 2.

3.1. Preprocessing Strategy of GNSS Observations

The data quality is believed to be improved by preprocessing GNSS observations, which is essential for extracting scintillation indices accurately. The preprocessing strategies include the excessive short arc rejection, the satellite elevation angle control, and the cycle slip detection (Zhao, Li, Li, et al., 2022). Considering that the length of the moving window is 60s, it is reasonable to remove any observation arcs that are less than 60 epochs. The satellite elevation angle is set to 30° to avoid the adverse effect of multipath. For the observations collected at three carriers, cycle slips are detected and fixed utilizing the Hatch–Melbourne–Wübbena (HMW) combinations (Zhao, Hancock et al., 2019, Zhao, Roberts et al., 2019). For the observations collected at dual-frequency, the epoch-differenced ionosphere-free (IF) combination is adopted to detect cycle slips. Instead of correcting cycle slips of the dual-frequency observations, the epoch with a cycle slip is taken as the start of a new arc, as IF cannot provide the magnitude of the cycle slip directly.

3.2. Geodetic Detrending

Most of the error sources, which affect the accuracy of the scintillation index extracted from 1 Hz GNSS carrier phase observations, can be eliminated using the existing formulas, models, and public parameters. This process is named as the GD (Juan et al., 2017). Table 1 summarizes strategies utilized in this paper to conduct the GD. However, the methods listed in this table cannot eliminate the tropospheric wet delay and the receiver clock error, where the extended research is conducted as follows.

The static PPP method is utilized to estimate the tropospheric wet delay. The basic observation in the PPP adopts the IF combination constructed with residuals of the GD. The parameters to be estimated in the PPP are the

Table 1
Strategies to Conduct Geodetic Detrending

Items	Processing strategies
Geometric distance	Static precision point positioning (PPP) solution, International GNSS Service (IGS) precise ephemeris product
Solid Earth tide	The second-order simplified tide model
Satellite and receiver antenna correction	IGS satellite and ground antenna calibrations (igs14.atx)
Satellite clock	IGS precise clock product
Phase wind-up	Wu et al. (1992)
Relativistic effect	Beard and Senior (2017)
Tropospheric zenith hydrostatic delay	GPT2 (Lagler et al., 2013)

coordinates of the station, the zenith tropospheric wet delay and the receiver clock error, which can be estimated by a Kalman filter. In order to improve the estimation accuracy, a forward and backward calculation is adopted and the outputs provided by the backward calculation are taken as the final solution. The estimated zenith tropospheric wet delay is converted to the slant path of each satellite by the Global Mapping Function (Boehm et al., 2006), so as to correct the tropospheric delay error in the observations regarding the original observation equation of the carrier phase measurement.

The receiver clock error is estimated and corrected utilizing the epoch-differenced IF combination, denoted as follows,

$$\Delta \hat{r}_{IF} = c \cdot \Delta \delta t_R + \Delta I_{IF}^d \quad (7)$$

where Δ is the time-differenced operator between two adjacent epochs; \hat{r}_{IF} denotes the residuals of IF combination; c is the speed of light in vacuum; δt_R is the receiver clock offset; ΔI_{IF}^d denotes the variation rate of ionospheric scintillation error, which can be ignored as its magnitude is usually small. Equation (7) can eliminate nearly all the error sources and provide the residual, which only contains the receiver clock error. However, for most geodetic receivers, when the receiver clock drifts to a certain threshold, a clock jump will be inserted to the clock, in order to synchronize the internal receiver clock and the GNSS time within a certain range. Before implementing Equation (7) to estimate the receiver clock error, the clock jump needs to be identified and corrected based on the output of the previous PPP process, as the clock jump is typically in the magnitude of 1 ms, much larger than other error sources, for example, the tropospheric delay and the ionospheric delay. After the correction of the clock jump, the residual of the time-differenced IF combination given by Equation (7) can be used to represent the variation of the receiver clock over time.

In order to improve the accuracy of the estimated receiver clock, all the satellite observations in each epoch above the cutoff angle are averaged with the following weight,

$$P = \sin^2 e \quad (8)$$

where P represents the weight. The weighted epoch-differenced receiver clock error can be expressed as follows,

$$\Delta \delta t_R(i) = \frac{1}{c} \cdot \frac{\sum_{s_n=1}^m \Delta \hat{r}_{IF_{s_n}} \cdot P_{s_n}}{\sum_{s_n=1}^m P_{s_n}} \quad (9)$$

where m represents the number of adopted satellites at epoch i ; s_n is the satellite number. The receiver clock error at the initial epoch is set to 0 s. On the basis of Equation (9), the receiver clock error at i th epoch is the integration of the weighted epoch-differenced receiver clock error between the initial epoch to i th epoch. This estimated value can be used to fix the receiver clock error in each individual frequency regarding the original observation equation of the carrier phase measurement.

3.3. Ionospheric Phase Scintillation Index Estimation With Continuous Wavelet Transform

The residual of the GNSS carrier phase observations after GD and cycle slip detection can be denoted as follows,

$$\hat{r}_f = I_f^r + I_f^d + B_f + \lambda_f N_f + \epsilon_f \quad (10)$$

where \hat{r}_f denotes the residual of the frequency f ; I_f^r and I_f^d denote the ionospheric refraction and scintillation signal respectively; B_f represents the hardware delay; λ_f is the wavelength; N denotes the ambiguity and ϵ_f is the measurement noise. The hardware delay and the ambiguity are constant values in one observation arc. Considering the frequency differences of different parameters in Equation (10), the continuous wavelet transform (CWT) can be utilized to extract the scintillation signal.

The CWT is a joint function of a time series signal and a wavelet, denoted as follows,

$$W(t, s) = \frac{1}{2\pi} \int_{-\infty}^{\infty} \Psi(s\omega) X(\omega) e^{i\omega t} d\omega \quad (11)$$

where W represents the wavelet transform coefficients; t and s denote the time and the scale respectively; $\Psi(\omega)$ represents the Fourier transform of the wavelet and $X(\omega)$ is the Fourier transform of the residual provided by Equation (10). The CWT can isolate the signal variability both in time and scale, by rescaling and shifting the analyzing wavelet, making it be good at localizing transients in nonstationary signals (Lilly & Olhede, 2009; Torrence & Compo, 1998), for example, ionospheric scintillations, as the ionospheric scintillation signal fluctuates at a higher frequency than the ionospheric refraction signal (Juan et al., 2017). The Morse wavelet is adopted in this paper. The Fourier transform of the Morse Wavelet is as follows,

$$\Psi_{\beta,\gamma}(s\omega) = U(\omega)\alpha_{\beta,\gamma}\omega^\beta e^{-\omega^\gamma} \quad (12)$$

where γ and β are named as the symmetry parameter and the time-bandwidth product of the Morse wavelet; $U(\omega)$ represents the Heaviside step function; $\alpha_{\beta,\gamma}$ is a normalizing constant. The detailed explanation on the parameterization of Morse wavelet refers to (Lilly & Olhede, 2009; Olhede & Walden, 2002). The shape of the wavelet is controlled by γ and β together. The central portion of the wavelet is broadened and the rate of the time decay is increased with a long time-bandwidth, while the wavelet envelope can be broadened without changing the time decay by increasing the symmetry parameter. Overall, the symmetry parameter and the time-bandwidth product affect the estimation of the scintillation index. The method to selecting the optimal symmetry parameter and the time-bandwidth product for extracting the scintillation signal will be provided in Section 3.5.

After the CWT computation, the residual of Equation (10) is transformed to the time-frequency matrix, where the coefficients corresponding to ionospheric scintillations are usually located in the middle frequency range, named as the characteristic frequency range of ionospheric scintillations. The upper and lower boundaries of the characteristic frequency range are called the upper boundary frequency and the lower boundary frequency, which are selected as 0.1 and 0.4 Hz respectively in this paper, as shown in Panel c of Figure 3. The coefficients

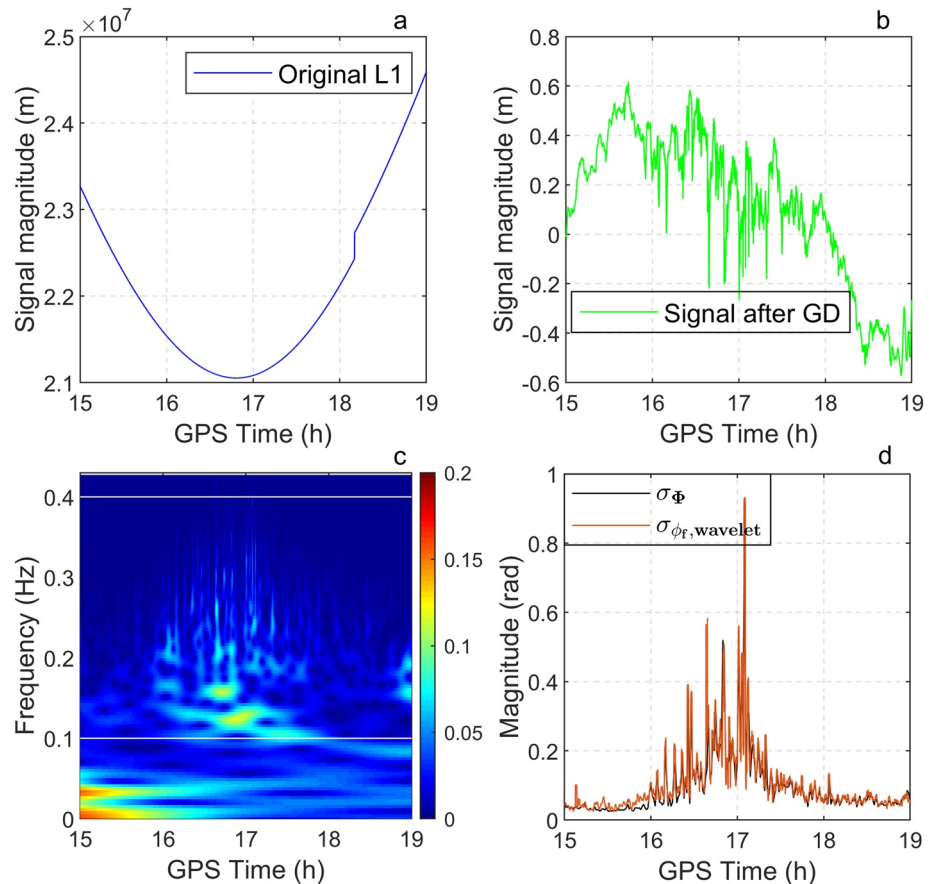


Figure 3. Illustration on the variation from the original GPS L1 carrier observations to the scintillation index.

located within the characteristic frequency range of ionospheric scintillation are used to extract the ionospheric scintillation signal, by utilizing the inverse continuous wavelet transform (ICWT). The detailed method to implementing ICWT refers to Liu et al. (2015). Based on the ionospheric scintillation signal, the phase scintillation index extracted from 1 Hz geodetic GNSS measurements can be obtained as follows,

$$\sigma_{\phi, \text{wavelet}} = \sqrt{\langle I_f^{d^2} \rangle - \langle I_f^d \rangle^2} \quad (13)$$

where $\sigma_{\phi, \text{wavelet}}$ is the extracted phase scintillation index. 60s is selected as the time interval for calculating Equation (13) using 1s-sampling-interval observations. The threshold for the extracted scintillation index is the same as that adopted by σ_{ϕ} , namely the phase scintillation index of ISMR.

3.4. An Example Illustrating the Outputs of the Above Steps

In order to help readers easier understand the proposed scintillation extraction method, Figure 3 illustrates the variation from the original 1s-sampling-interval GPS L1 carrier observations to the final scintillation index. As shown in Panel a, the observations from 15 to 19hr of PRN07 on the day 111 of the year 2020 at the station arcc are adopted to conduct this illustration. The residual after GD, namely the output of Equation (10), is displayed in Panel b. The signal is transformed with the Morse wavelet, in which the obtained coefficients are visualized in Panel c of Figure 3. This panel is called the time-frequency spectrum, which displays the variation of the absolute value of the wavelet coefficients (W) obtained from Equation (11), with regards to both the frequency and the time. It can be seen from the time-frequency spectrum that large modulus values are mainly concentrated below 0.1 Hz, corresponding to the ionospheric refraction effect of this observation arc, while several large modulus values in the middle frequency range, namely the area between the two white lines in Panel c, mainly correspond to the characteristic frequency range of the ionospheric scintillation, which shows that the Morse wavelet has the ability to extract ionospheric scintillation signals in the time-frequency domain. Finally, the scintillation index, shown in Panel d, is obtained by calculating Equation (13) based on the signal given by applying ICWT to the coefficients within the characteristic frequency range.

3.5. Determination of the Symmetry Parameter and the Time-Bandwidth Product for the Morse Wavelet

In order to determine the search space of the symmetry parameter and the time-bandwidth product for the Morse wavelet, a special case study is conducted using one observation arc affected by scintillations to test the performance of two parameter groups with a farther distance, for example, (3,60) and (6,20), where the two parameters in the bracket represent the symmetry parameter and the time-bandwidth product respectively. The method to conduct this case study is as follows. First, the scintillation index is extracted with the two parameter groups. Then, the correlation, the slope of the linear fitted line and the root mean square (RMS) of the residual between the extracted scintillation index and the reference, namely the σ_{ϕ} index provided by ISMR, are calculated for the following analysis. A higher correlation means a higher similarity between the estimated scintillation index and the reference. The slope of the linear fitted line measures the number of units the $\sigma_{\phi, \text{wavelet}}$ index goes up for every unit the σ_{ϕ} index is moved to the right, which means the value of the slope being equal to 1 can indicate that the magnitude of the $\sigma_{\phi, \text{wavelet}}$ index is basically the same as that given by the σ_{ϕ} index. The RMS of the residual measures the differences between the $\sigma_{\phi, \text{wavelet}}$ index and the σ_{ϕ} index. A smaller RMS value can reveal the $\sigma_{\phi, \text{wavelet}}$ index being more accurate.

Figure 4 presents the results of the special case study. As shown in Panels a and b, the accuracy of the estimated scintillation index varies with the symmetry parameter and the time-bandwidth product. Panels c and d show that the correlation is higher and the slope of the linear fitting is closer to one when using (3,60). The RMS of the residual (see Panels e and f) is greater with (6,20), especially during the period with scintillations. The slope obtained by (3,60) is greater than 1, while that given by (6,20) is less than 1. Therefore, it is reasonable to suppose that the proper parameter group might be between these two parameter groups.

On the basis of the potential search space of the proper parameter group, the observations collected at all the 11 ISMR stations in the year of 2020 are adopted to decide the proper parameter group with the following method. First, the symmetric parameter is selected from 3 to 6 with 1 as the step, while the time-bandwidth product is

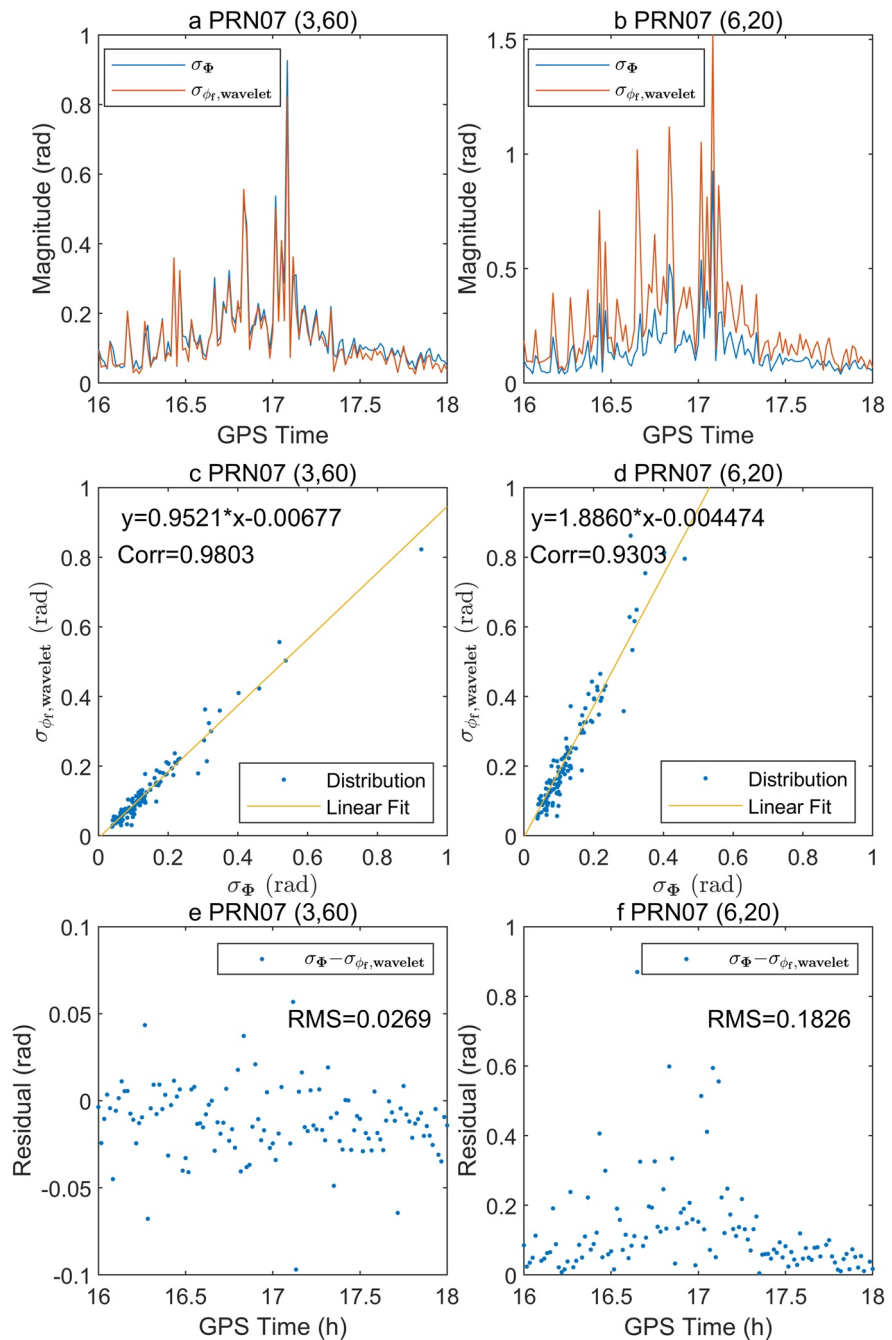


Figure 4. Special case analysis of two parameter groups (3,60) and (6,20) for Morse wavelet using the observation arc from PRN07 collected on the day 111 of 2020 at the station arcc. The two parameters represent the symmetry parameter and the time-bandwidth product respectively. Panels a and b: comparison between the reference and the scintillation index extracted by the corresponding parameters; Panels c and d: the linear fitted lines and the correlation analysis; panels e and f: residual analysis.

chosen from 20 to 60 in the step of 5, forming a variety of parameter groups. Then the scintillation index is estimated using these parameter groups. Lastly, a statistical analysis is conducted regarding the mean and the STD values of the following three indicators, for example, the slope of the linear fit, the correlation and the RMS of the residual between the estimated scintillation index and the reference. The statistical analysis pays special attention to the periods with scintillations, as the difference of the magnitudes estimated from different parameters can be

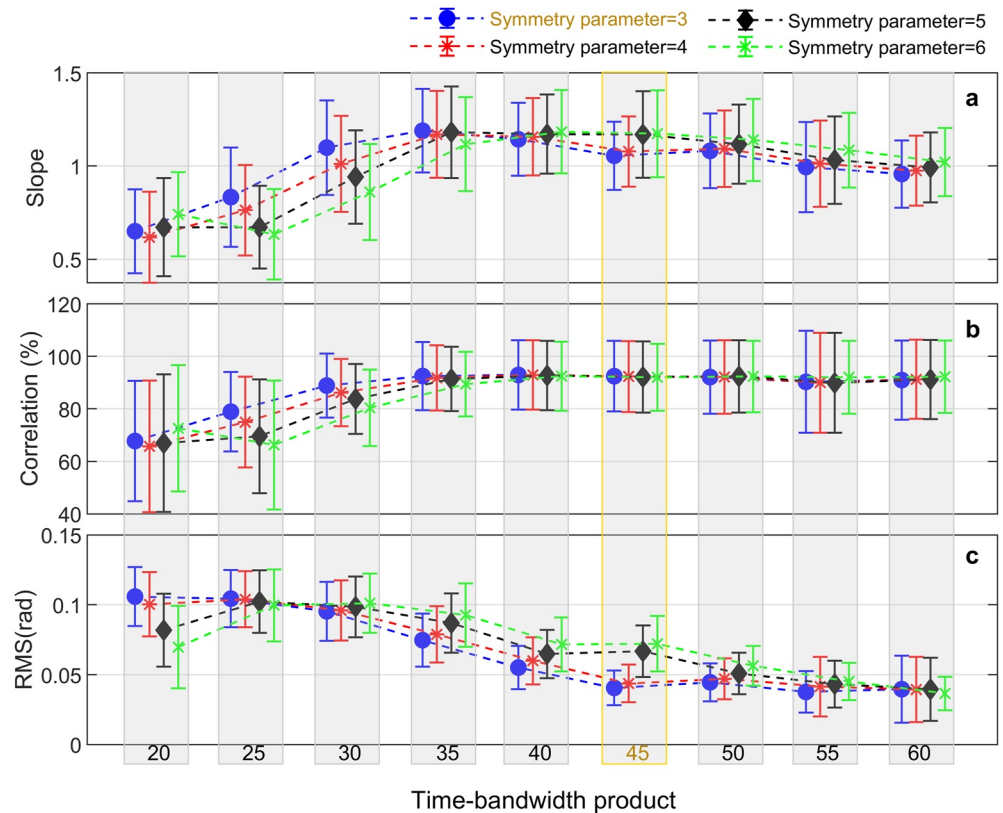


Figure 5. Statistical analysis of the mean value of the linear fitting slope, correlation and residual between the reference and the scintillation index constructed by different symmetry parameters and time-bandwidth products during periods with scintillations ($\sigma_{\phi} \geq 0.2\text{rad}$). The error bar represents the standard deviation. The optimal symmetry parameter and the time-bandwidth product are marked with the golden color.

negligible during the periods without scintillations (see the scintillation index during 17.5–18 in Panels a and b of Figure 4).

Figure 5 presents the variation of the above three indicators during periods with scintillations. The fluctuation of each indicator under the corresponding parameter combination is represented by the STD, as shown by the error bar. In the period with scintillation, the symmetry parameter 3, together with the time-bandwidth product 45, 50, 55 or 60, can provide the best performance, which are approximately 1 for the slope, 0.92 for the correlation and 0.03 rad for the RMS of the residual. As a large time-bandwidth product increases the complex waveform of the wavelet, affecting the calculation efficiency of the ionospheric scintillation index greatly, this paper selects (3,45) as the optimal symmetry parameter and time-bandwidth product for Morse wavelet.

4. Scintillation Monitoring Performance of the $\sigma_{\phi_f, \text{wavelet}}$ index

The scintillation monitoring performance of the $\sigma_{\phi_f, \text{wavelet}}$ index is analyzed using the observations collected in the year of 2020. The scintillation monitoring performance is evaluated considering the magnitude accuracy in each observation arc, the detected daily scintillation occurrence rate, the diurnal variation pattern of the ionospheric scintillation, the correlation with the space weather parameter, and the distribution of the magnitude. If the scintillation monitoring performance of the $\sigma_{\phi_f, \text{wavelet}}$ index is consistent with that provided by the reference, it is reasonable to believe the extracted scintillation index is accurate and stable. This section displays the results from the 1s-sampling-interval observations collected at the five stations as examples, including two high-latitude ISMR stations (arcc and kugc), two middle-latitude ISMR stations (fsmc and chuc) and one middle-latitude station with a geodetic receiver (chur).

It should be noted that the adopted Septentrio receivers only provide the σ_ϕ index at the L2C signal, which was only available at around half of the GPS constellation in 2020. In order to avoid the scintillation pattern difference due to the unequal number of GPS L2 satellites adopted by different scintillation indices, only the results obtained by GPS L1 signal are displayed in this section. Considering the ionospheric scintillation in the high-latitude region has similar effect on different GNSS signals, observations from GPS L1 signal are sufficient to validate the $\sigma_{\phi_f, \text{wavelet}}$ index.

4.1. Magnitude Details of the $\sigma_{\phi_f, \text{wavelet}}$ index Extracted From the Observation Arcs Affected by Scintillations

As many other wavelets can also be adopted to conduct the time-frequency analysis of the CWT, the magnitude details of the $\sigma_{\phi_f, \text{wavelet}}$ index extracted with the Morse wavelet are first compared with those provided by another two widely used wavelets, namely the analytic Morlet wavelet and the Bump wavelet. Panel a of Figure 6

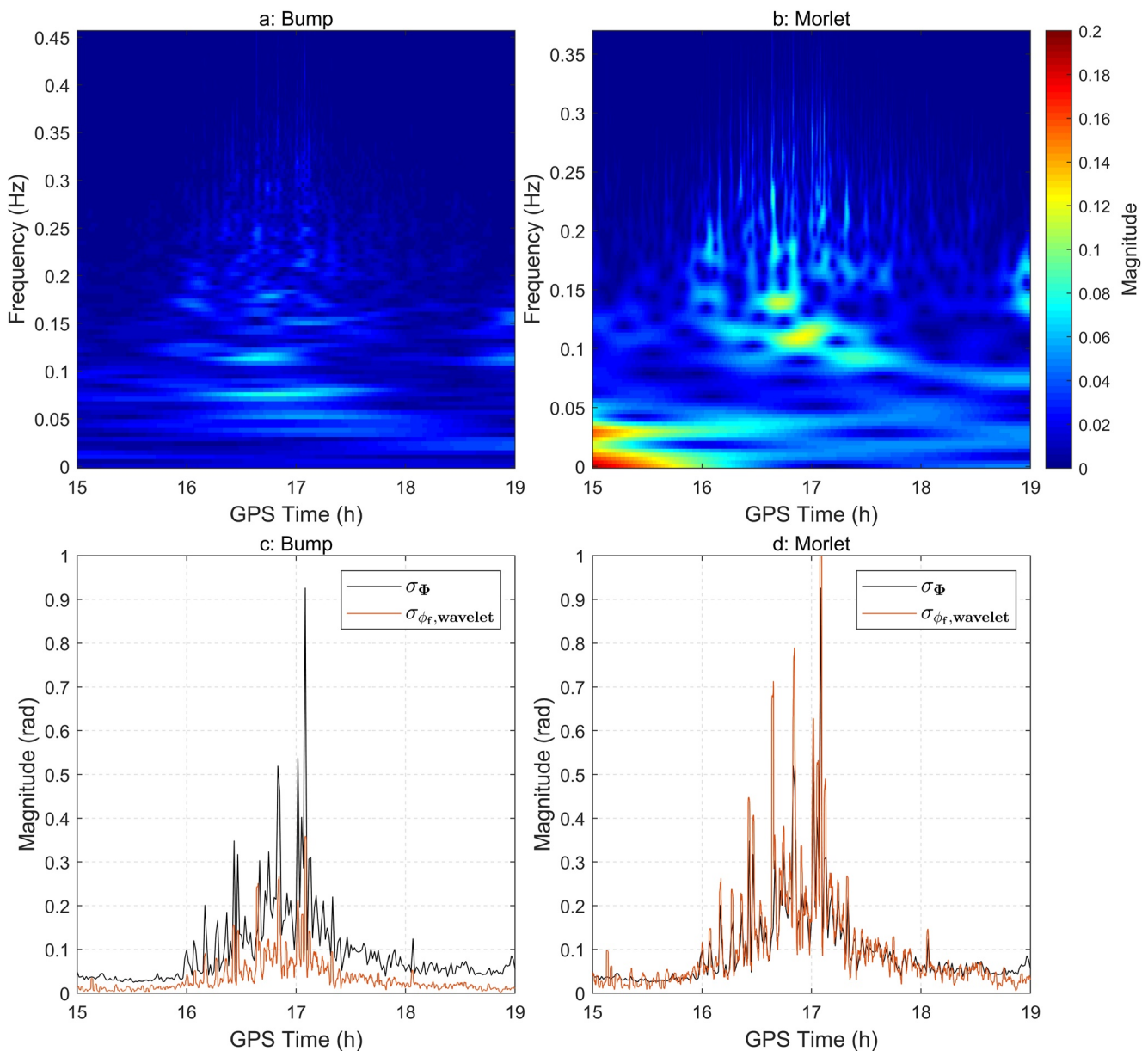


Figure 6. The time-frequency spectrum (Panels a, b) and the corresponding scintillation index (Panels c, d) extracted with the Bump and Morlet wavelets respectively based on the observation arc collected from 15 to 19hr of PRN07 on the day 111 of the year 2020 at the station arc.

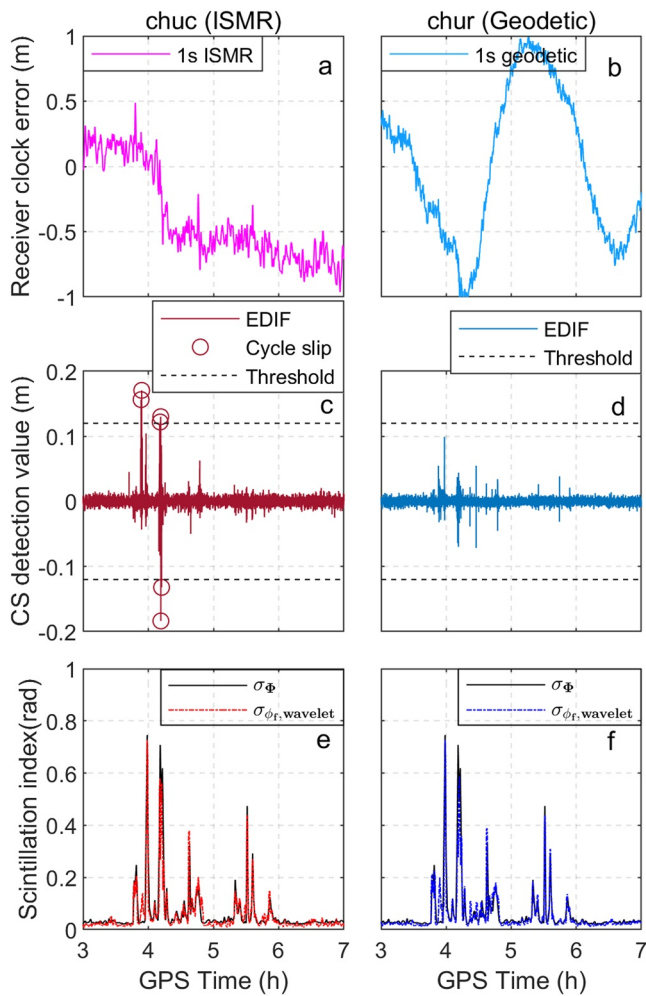


Figure 7. Comparison between the scintillation index extracted from the 1s-sampling-interval observations collected at the station chuc with an Ionospheric Scintillation Monitoring Receivers and that at the station chur with a geodetic receiver. CS and EDIF denote the cycle slip and the epoch-differenced ionosphere-free combination respectively.

the $\sigma_{\phi_f, \text{wavelet}}$ index. Although this threshold might not be the optimal, the results in Panels e and f confirm the applicability of this threshold in extracting the scintillation index. Comparing the cycle slip detection results in Panels c and d, no cycle slip is detected in the observation arc from the station chur, however small outliers occur more frequently in the detection value of the geodetic receiver than that of the ISMR, indicating the carrier phase of a geodetic receiver is more susceptible to ionospheric scintillations. These unexpected small outliers lead to several inaccurate magnitudes of the extracted scintillation index, such as the scintillation index at around 3:55 and 4:30 in Panel f. Despite these several inaccurate magnitudes, they will not affect the judgment of the scintillation occurrence in this observation arc on account of the 0.2 rad as the scintillation threshold. Generally, both the scintillation index from the 1s-sampling-interval ISMR and geodetic receiver observations can be considered as accurate at the epoch level, compared to the σ_{ϕ} index. The analysis of this figure reveals that the proposed method can extract the scintillation index accurately from the 1s-sampling-interval observations of the geodetic receiver, with the parameters determined based on the down-sampled ISMR observations.

In order to further quantitatively measure the accuracy of the estimated scintillation index, we calculate the correlation between the $\sigma_{\phi_f, \text{wavelet}}$ index and the σ_{ϕ} index at each observation arc. As the difference between the

shows that the ionospheric scintillation signals cannot be clearly visible in the time-frequency spectrum of the Bump wavelet, which might be for the reason that the frequency response range of the Bump wavelet cannot cover the whole frequency range of the ionospheric scintillation, resulting in the scintillation index extracted with the Bump wavelet being significantly lower than that given by ISMR, as shown in Panel c. Although the time-frequency spectra of both the Morlet wavelet and the Morse wavelet can generally reflect the information of the ionospheric scintillation signal (see Panel b of Figure 6 and Panel e of Figure 3), the magnitude of the ionospheric phase scintillation index obtained by the Morlet wavelet is significantly larger than the reference, while that given by the Morse wavelet is basically equivalent to the reference value (see Panel d of Figure 6 and Panel f of Figure 3). Overall, the Morse wavelet can be expected to extract more accurate scintillation index from 1s-sampling-interval GNSS observations than the Bump or Morlet wavelet.

As the optimal symmetry parameter and the time-bandwidth product are determined with the 1s-sampling-interval observations filtered from the 1/50s-sampling-interval data of the ISMR, this section verifies the usability of the proposed method and the corresponding parameters in extracting the scintillation index from the geodetic receiver. Figure 7 displays the receiver clock error, the cycle slip detection value and scintillation indices extracted by applying the proposed method to the observations from an ISMR (the station chuc) and a co-located geodetic receiver (the station chur) respectively. The data is collected from PRN 21 during 3–7h on the day 111 of the year 2020.

Panels a and b of Figure 7 reveal that the receiver clock error of the geodetic receiver is less stable compared to that of the ISMR. Results of the cycle slip detection (see Panels c and d) show that the adopted detection value, namely the time-differenced IF combination, is precise enough in detecting cycle slips for the purpose of extracting scintillation index, although the receiver clock error was not fixed before cycle slip detection. It can also be seen from Panels c and d that the outliers in the detection value mainly occur during the periods with scintillations, which cause the variation of the carrier phase. The threshold of the cycle slip detection value can determine the magnitude of the outlier which is to be fixed as a cycle slip or remained as the scintillation information propagated to the $\sigma_{\phi_f, \text{wavelet}}$ index. Considering 1 rad in L1 carrier corresponds to 0.12 m in the IF combination, 0.12 m is selected as the threshold for cycle slip detection, to avoid the over-large magnitude in

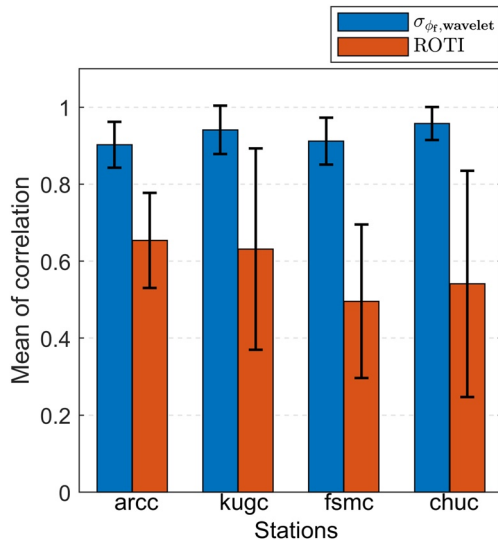


Figure 8. Mean and standard deviation of the correlations between the σ_{ϕ} index (or the Rate of Total electron content Index) and the σ_{ϕ} index obtained from the observation arcs affected by scintillations.

σ_{ϕ} index and the σ_{ϕ} index can be negligible during the period without scintillations (see the results during 6–7h in Panel e of Figure 7), we only present the correlation results obtained from the arcs with scintillations. Figure 8 displays the mean and the STD values of the correlations obtained at the stations arcc, kugc, fsmc and chuc. It can be seen that the correlations between the σ_{ϕ} index and the σ_{ϕ} index can provide a much higher mean with a smaller STD than those between the ROTI and the σ_{ϕ} index. This reveals that the magnitude of the σ_{ϕ} index is generally more consistent with the σ_{ϕ} index than the ROTI.

4.2. Detected Daily Scintillation Occurrence Rate of the σ_{ϕ} index

This section is to test whether the σ_{ϕ} index can provide the accurate daily scintillation occurrence rate, which is defined as follows,

$$R = \frac{N_s}{N_t} \times 100\% \quad (14)$$

where R denotes the daily scintillation occurrence rate; N_s is the total number of epochs where the ionospheric scintillation index is greater than the threshold; N_t is the total number of epochs in a day.

The daily scintillation occurrence rate is related to the threshold for the ionospheric scintillation, while the threshold is determined with the magnitude of the scintillation index. The magnitude of the σ_{ϕ} index is at the same level as that of the σ_{ϕ} index (see Panels e and f of Figure 7), making the 0.2 rad can be applied as the threshold for the σ_{ϕ} index as well, while the magnitude of ROTI can be significantly different from that of the σ_{ϕ} index (Zhao, Li, Li, et al., 2022). Generally, 0.1 TECU/min is suggested as the threshold for the ROTI calculated from 30s-sampling-interval observations with a 5-min moving window (Ma & Maruyama, 2006), while existing research failed to provide the experienced threshold for the ROTI calculated from 1s-sampling-interval observations with a 1-min moving window. This paper determines the threshold for ROTI as follows. First, the proportion of the epochs with the σ_{ϕ} index above the threshold is obtained for the whole year observations at each station. It is assumed that ROTI can provide the same proportion of scintillation as the σ_{ϕ} index at the annual level. Then the threshold of ROTI at each station can be determined as the magnitude corresponding to the same proportion of scintillation in the complementary cumulative distribution function of the ROTI calculated with the whole-year observations. With this method, 0.0482, 0.0562, 0.0517, and 0.0570 TECU/min are determined as the thresholds for the stations arcc, kugc, fsmc and chuc respectively.

The left four panels of Figure 9 present the daily scintillation occurrence rates detected by the σ_{ϕ} , σ_{ϕ} and ROTI indices, while the right panels display the distributions of the rate differences, namely $R(\sigma_{\phi}) - R(\sigma_{\phi})$ and $R(\text{ROTI}) - R(\sigma_{\phi})$. The right four panels show that about 95% of the rate differences are distributed within $\pm 0.5\%$ for both σ_{ϕ} and ROTI. Compared to ROTI, the rate differences given by the σ_{ϕ} index are allocated higher within the range of $\pm 0.05\%$, indicating that the σ_{ϕ} index can be believed to perform scintillation monitoring more accurately.

The left four panels of Figure 9 reveal that the daily ionospheric scintillation occurrence rates provided by the σ_{ϕ} index meet well with the σ_{ϕ} index during the whole year for both the 1s-sampling-interval ISMR and geodetic receiver observations, while the daily scintillation occurrence rates of about the last 80 days at the station arcc given by the ROTI are much lower than those given by both the σ_{ϕ} and the σ_{ϕ} indices, as shown in Panel a of Figure 9. One possible reason leading to this phenomenon might be due to the high-frequency fluctuations of satellite clocks (Nguyen et al., 2019). The proposed scintillation extraction method eliminates the effect of the satellite clock error by applying the IGS precise clock product, which is a smooth value of the satellite clock variation over a period time, thus losing the ability to capture the high-frequency fluctuations of satellite clocks. This satellite clock error will propagate and contaminate the estimation of the receiver clock, hence making the rapid fluctuation in the σ_{ϕ} index. Similarly, this mismodeled fluctuation cannot be canceled out by the

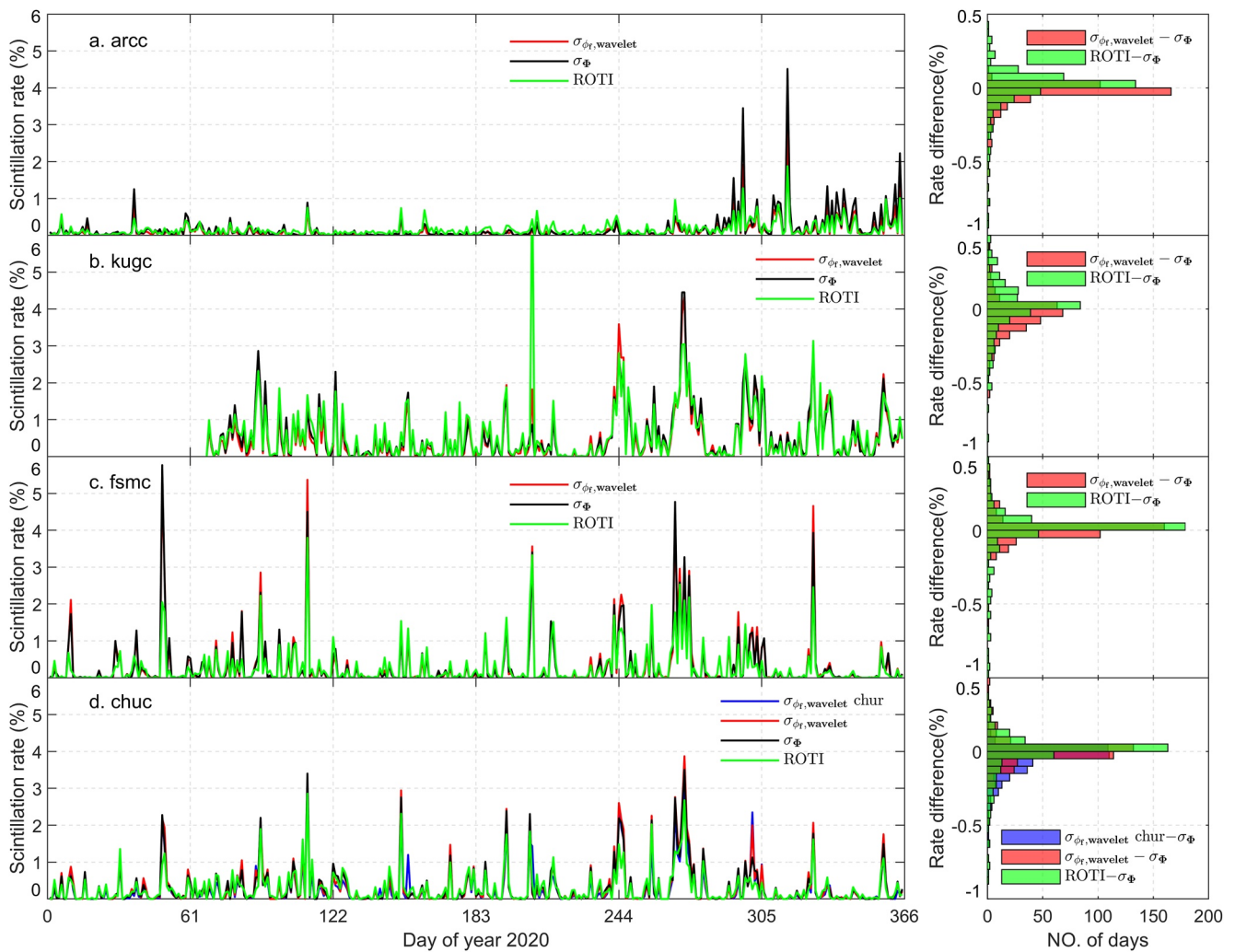


Figure 9. Daily ionospheric scintillation occurrence rate detected in the whole year of 2020 (left four panels), and the rate differences (right four panels). The bin width in the right panels is 0.05%.

high-pass filter of the ISMR and thus distorts the σ_{ϕ} index. However, the satellite clock error can be canceled out in the GF combination, making the ROTI be not affected by the high-frequency fluctuation of satellite clocks. Another reason is that the code-encrypted L2 (L2W) signal is obtained from the L1C signal in the Septentrio receivers (McCaffrey et al., 2018), making part of the high-variation ionospheric effect in the L1C signal be presented in L2. This propagated ionospheric fluctuating information can be eliminated in the GF combination calculated with the L1-aided L2 signal, resulting in the low values of ROTI and also the low daily scintillation occurrence rates in the last 80 days at the station arcc.

4.3. Diurnal Variation Pattern of the Ionospheric Scintillation Detected by $\sigma_{\phi_f, \text{wavelet}}$

Due to the effect of the local solar angle, the occurrence of the ionospheric scintillation presents a diurnal variation pattern (Jiao & Morton, 2015; Karatay, 2020). The performance of $\sigma_{\phi_f, \text{wavelet}}$ will be evaluated in detecting this diurnal variation pattern as follows (Zhao, Li, Li, et al., 2022). The astronomical algorithm is first applied to obtain the local time of each station (Meeus, 1998). Then, the number of epochs with scintillations is statistically counted in each hour after local sunset at each station. The scintillation occurrence probability is defined as the ratio between the total number of epochs with scintillations in each hour and that in the whole year. The diurnal variation pattern of the ionospheric scintillation is represented by the changes of the scintillation occurrence probability for each hour of a day in this paper. Due to the phenomena of polar days and polar nights, the

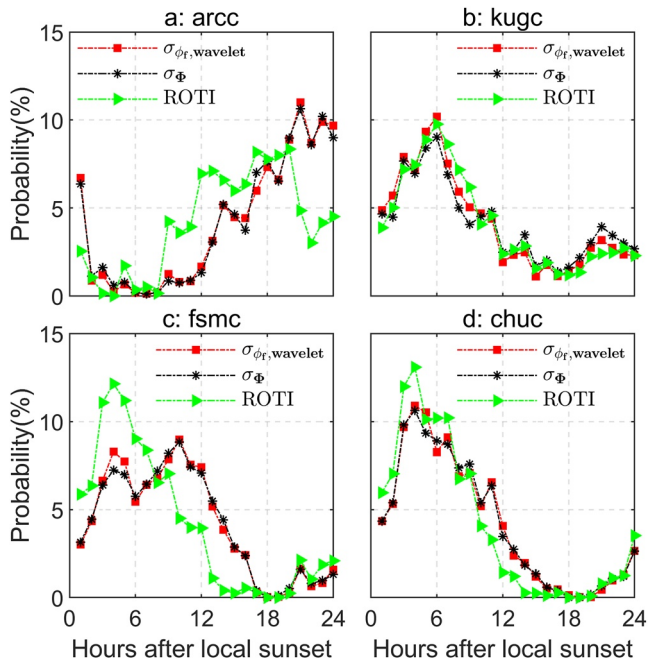


Figure 10. Scintillation occurrence probability with respect to hours after local sunset.

observations collected during the local summer and the local winter of the stations arcc and kugc will be studied separately regarding the local time, instead of the hours after local sunset.

Figure 10 presents the diurnal occurrence pattern of ionospheric scintillation regarding the hours after local sunset. From the results given by the σ_ϕ index, the occurrence of the ionospheric scintillation follows the characteristic with one peak occurring at different time for the stations arcc, kugc and chuc. For the station arcc, the ionospheric scintillation occurrence peak occurs within 6 hr before sunset, while the peak occurs approximate 6 hr after sunset at the stations kugc and chuc. The station fsmc observes two occurrence peaks, in which one lower peak occurs within 6 hr and the other higher peak occurs in 6–12 hr after sunset. The $\sigma_{\phi_f, \text{wavelet}}$ index can detect this occurrence pattern. ROTI provides inaccurate peak occurrence time and occurrence probability at the stations arcc and chuc respectively, and fails to detect the second peak at the station kugc.

Figure 11 shows the scintillation occurrence probability during the local summer and the local winter at the stations arcc and kugc. When the polar night phenomenon occurs (see Panels b and d), two scintillation occurrence peaks can be observed, and the occurrence times of the peaks are similar for the two stations, both at the local midnight and noon. During the local summer (see Panels a and c), the result of the σ_ϕ index shows that one scintillation occurrence peak can be observed at the local noon for the station arcc and the local midnight for the station kugc. The reason leading to the different patterns at the two stations might be due to the latitude of the stations. The station arcc is located in the polar cusp region, where the magnetic field intensity is almost zero, allowing the solar wind to enter the upper atmosphere unimpeded, hence scintillations occur more frequently at the local noon. The ionospheric scintillation at the station kugc might be affected by the local geomagnetic field. More specific reasons for these different patterns are beyond the scope of this paper and will be left for future research. Regarding the validity of the $\sigma_{\phi_f, \text{wavelet}}$ index, it can detect the scintillation occurrence pattern during both the local summer and the local winter at both stations, while ROTI fails to detect the occurrence peak at the local noon of the station kugc and provides a lower occurrence probability at the local noon of the station arcc compared to the σ_ϕ index during the local winter.

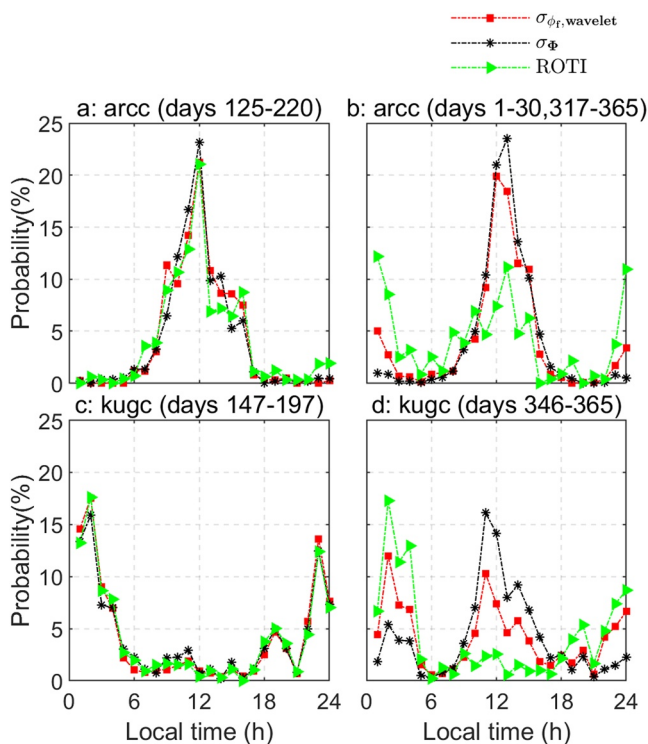


Figure 11. Scintillation occurrence probability during the local summer (Panels a and c) and the local winter (Panels b and d) at the stations arcc and kugc. The specific days for these periods are shown in the title of each panel.

4.4. Correlation Between the Scintillation Occurrence Rate and the Space Weather Parameters

Space weather refers to conditions on the sun and in the solar wind, magnetosphere, ionosphere, and thermosphere that can influence the performance and reliability of space-borne and ground-based technological systems and can endanger human life or health (Khazanov, 2016). As a result of space weather disturbances, the electron density of the ionosphere along receivers' line-of-sight varies rapidly, making the ionospheric scintillation be closely related to interplanetary magnetic fields and geomagnetic field disturbances, especially in high-latitude regions (Amaechi et al., 2021; Fathy & Ghamry, 2021; Goldovsky & Luria, 2004; Maltseva & Nikitenko, 2021). Therefore, the correlation between the detected scintillation rate and the parameters of space weather condition, for example, Ap, can be further adopted to evaluate the performance of the $\sigma_{\phi_f, \text{wavelet}}$ index, as the correlation given by the $\sigma_{\phi_f, \text{wavelet}}$ index should be similar to that of the σ_ϕ index if the $\sigma_{\phi_f, \text{wavelet}}$ index can monitor scintillations accurately.

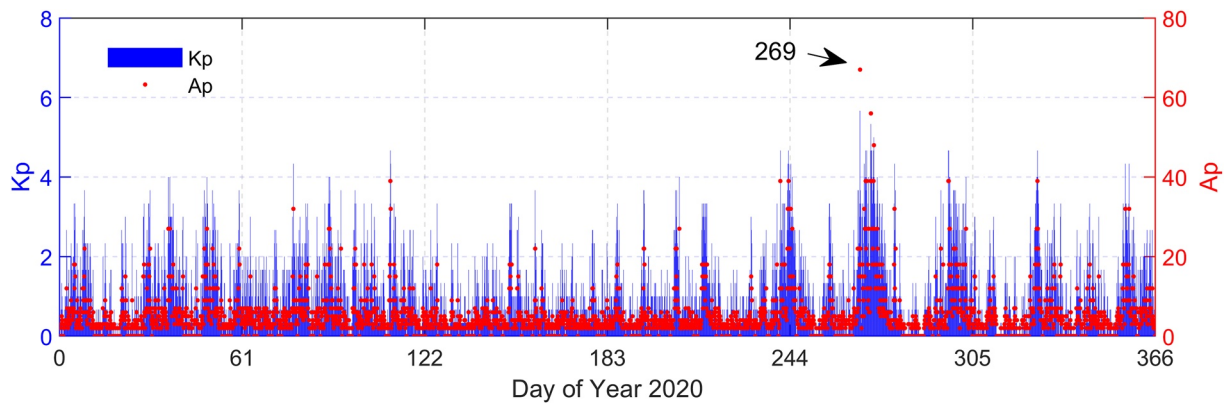


Figure 12. Space weather condition in the year of 2020.

The space weather condition in the year of 2020 is represented by the Kp and Ap indices in this paper, as shown in Figure 12. The Kp and Ap indices are provided with a resolution of three-hour, measuring solar particle radiation by its magnetic effects (Matzka et al., 2021). The year of 2020 is at the beginning of the 25th solar cycle, when the solar activities start to increase slowly. The most disturbed geomagnetic activity was occurred at the day 269, in which the magnitude of Kp reached 6.

The scatter diagram in Figure 13 presents the distribution of the daily scintillation occurrence rate with regards to the daily averaged Ap index, while the straight lines in this figure are the least squares fit to the distribution of the corresponding scintillation index. The values of the correlations are also listed in each panel. Results of

the σ_ϕ index shows that the correlations obtained at the stations kugc, fsmc and chuc, are higher than that given by the station arcc. The differences of the correlations between the $\sigma_{\phi_f, \text{wavelet}}$ index and the σ_ϕ index are smaller than those between ROTI and the σ_ϕ index at all the four stations, indicating the $\sigma_{\phi_f, \text{wavelet}}$ index is more accurate in detecting the scintillations caused by the geomagnetic activities.

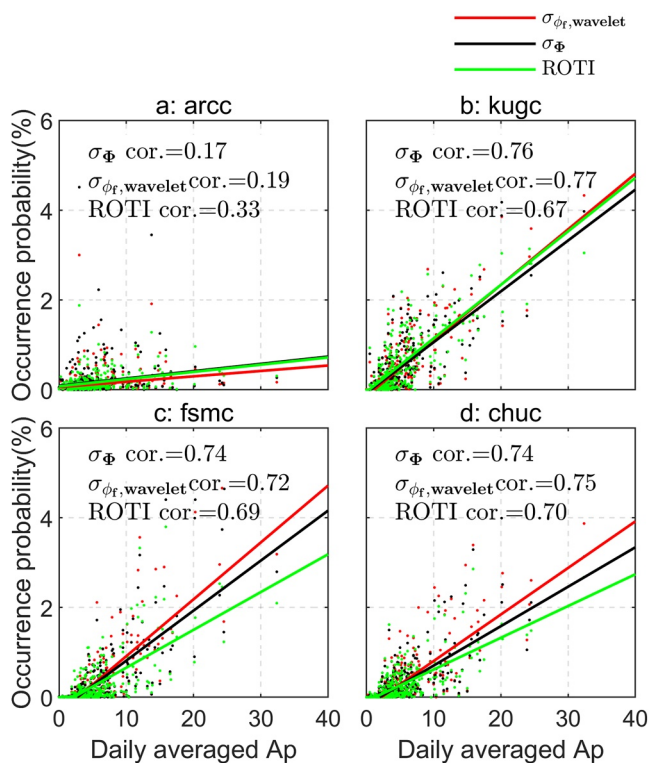


Figure 13. Distribution of scintillation daily occurrence rates and their least squares fitted lines with regards to the daily averaged Ap index. The “cor.” denotes the correlation.

Figure 13 also displays that the slope differences between the fitted lines of the σ_ϕ index and those of the ROTI are more significant at the low-latitude stations, compared to those at the high-latitude stations. A similar pattern can also be obtained in Figure 8, which shows that the correlations between the ROTI and the σ_ϕ index at the low-latitude stations are lower than those at the high-latitude stations. The reason leading to this pattern might be that the ionospheric scintillation is extracted in each carrier for the $\sigma_{\phi_f, \text{wavelet}}$ index, while ROTI extracts the scintillation in the GF combination. The phase fluctuations associated to scintillations in L1 and L2 carriers are quite correlated in the high-latitude region (Béniguel et al., 2009), making the scintillation in the GF combination have a close correlation with the scintillation on each carrier, while in the middle and low latitude region, scintillations on both carriers appear to be more uncorrelated due to the relevance of the signal diffraction, decreasing the consistency of ROTI (Juan et al., 2017). A smaller difference in the slope and a higher value of the correlation reveal a much higher consistency between the $\sigma_{\phi_f, \text{wavelet}}$ index and the σ_ϕ index.

4.5. Distribution of the Magnitudes Above the Threshold

The accuracy of the estimated scintillation index can be measured by the distribution of the magnitudes above the threshold, as the distribution should be consistent with that provided by the σ_ϕ index. Figure 14 presents the complementary cumulative distributions function (CCDF) of the σ_ϕ and $\sigma_{\phi_f, \text{wavelet}}$

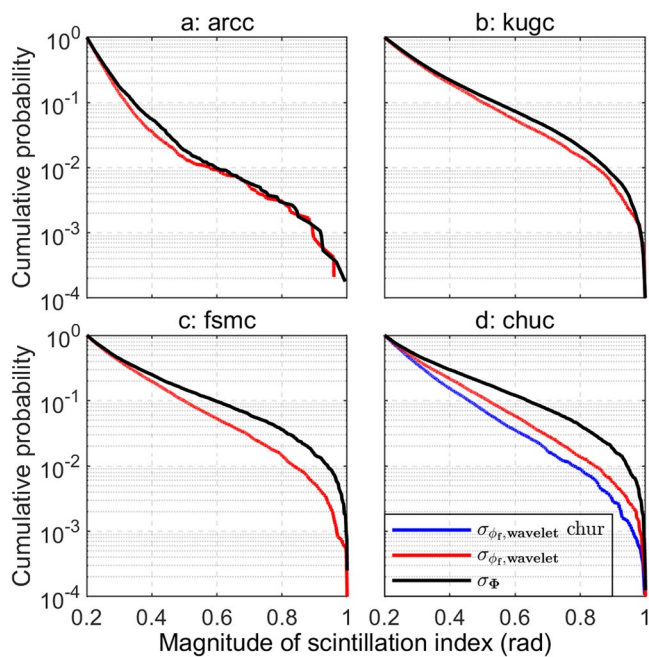


Figure 14. Distribution of the scintillation index above the threshold.

Acknowledgments

This study was supported by the National Natural Science Foundations of China (Nos. 41730109; 41874040; 42074226), the Natural Science Foundation of Jiangsu Province (Nos. BK20200664, BK20200646), the Fundamental Research Funds for the Central Universities (2020QN30, 2020QN31), Key Laboratory of Geospace Environment and Geodesy, Ministry of Education, Wuhan University (No. 20-01-09), the Open Research Fund of Key Laboratory of Land Environment and Disaster Monitoring, Ministry of Natural Resources, China university of mining and technology (No. LEDM2021B10), the National Key Research and Development Program of China (No. 2020YFA0713502), the Xuzhou Key Project (No. KC19111), the Priority Academic Program Development of Jiangsu Higher Education Institutions (PAPD), the Programme of Introducing Talents of Discipline to Universities (No. B20046) and the Jiangsu Dual Creative Doctors Project. We thank Joey Bernard from CHAIN for the personal emails confirming the clock failure of kugc station.

indices above the threshold using the 1s-sampling-interval data collected with both ISMR and the geodetic receiver. The CCDF is computed according to the method presented by Moraes et al. (2017). The CCDFs provided by the $\sigma_{\phi_f, \text{wavelet}}$ index are basically the same as those given by the σ_{ϕ} index at the high-latitude stations (arcc and kugc), while a bias can be observed between the CCDFs of the $\sigma_{\phi_f, \text{wavelet}}$ and the σ_{ϕ} indices at the middle-latitude stations (fsmc, chuc and chur), indicating the $\sigma_{\phi_f, \text{wavelet}}$ index can provide more accurate scintillation monitoring performance in the high-latitude region. As the bias does not exceed 3%, it is still reasonable to consider the extracted scintillation index be accurate at the middle-latitude stations equipped with either the geodetic receiver or ISMR set at 1s-sampling-interval.

5. Conclusions

This paper proposes a new method to extract the phase scintillation index from each carrier of 1s-sampling-interval GNSS observations through the excessive short arc rejection, the satellite elevation angle control, the cycle slip detection, the GD and the wavelet transform. The optimal symmetry parameter and the time-bandwidth product of the Morse wavelet transform are also determined considering the slope of the linear fitted line, the correlation and the residual between the extracted scintillation index and the σ_{ϕ} index in each observation arc.

Taken the σ_{ϕ} index provided by ISMR as the reference, the scintillation monitoring performance of the $\sigma_{\phi_f, \text{wavelet}}$ index is evaluated regarding the mean and STD values of the correlation in each observation arc, the detected daily scintillation occurrence rate, the diurnal variation pattern of the ionospheric scintillation, the correlation between the scintillation occurrence rate and the space weather parameter, and the complementary cumulative distribution of the magnitudes. The ROTI is adopted as a comparison. Results showed that a higher consistency can be achieved between the $\sigma_{\phi_f, \text{wavelet}}$ index and the σ_{ϕ} index, indicating the rationality of applying the $\sigma_{\phi_f, \text{wavelet}}$ index in monitoring scintillations.

Compared to the 1s-sampling-interval observations, GNSS data with 30s-sampling-interval is available more widely, for example, the globally distributed IGS stations. It is possible to realize the scintillation monitoring on a global scale if the 30s-sampling-interval observations can be introduced into the field of the ionospheric scintillation research. However, new challenges will be brought by the lower sampling rate. Therefore, extending the proposed method to extract the scintillation index from 30s-sampling-interval observations will be the potential research for the future.

Data Availability Statement

The 1 Hz GNSS observations and the scintillation index are available at the Canadian High Arctic Ionospheric Network (http://chain.physics.unb.ca/chain/pages/data_download). The data collected at the chur station is from Canadian Active Control System (<https://webapp.geod.nrcan.gc.ca/geod/data-donnees/cacs-scca.php#>). The Kp and Ap index can be downloaded from German Research Centre for Geosciences (<https://www.gfz-potsdam.de/en/kp-index/>), while the local geomagnetic field data and the f10.7 index are available at Natural Resources Canada (<https://geomag.nrcan.gc.ca/index-en.php>).

References

- Ahmed, A., Tiwari, R., Strangeways, H. J., Dlay, S., & Johnsen, M. G. (2015). Wavelet-based analogous phase scintillation index for high latitudes. *Space Weather*, 13(8), 503–520. <https://doi.org/10.1002/2015SW001183>
- Amaechi, P. O., Humphrey, I., & Adewoyin, D. A. (2021). Assessment of the predictive capabilities of NIGTEC model over Nigeria during geomagnetic storms. *Geodesy and Geodynamics*, 12(6), 413–423. <https://doi.org/10.1016/j.geog.2021.09.003>
- Beard, R., & Senior, K. (2017). Clock. In P. J. Teunissen & O. Montenbruck (Eds.), *Springer handbook of global navigation satellite systems* (pp. 121–164). Springer.

- Béniguel, Y., Adam, J. P., Jakowski, N., Noack, T., Wilken, V., Valette, J. J., et al. (2009). Analysis of scintillation recorded during the PRIS measurement campaign. *Radio Science*, 44(1), RS0A30. <https://doi.org/10.1029/2008RS004090>
- Béniguel, Y., Cherniak, I., Garcia-Rigo, A., Hamel, P., Hernández-Pajares, M., Kamení, R., et al. (2017). MONITOR ionospheric network: Two case studies on scintillation and electron content variability. *Annales Geophysicae*, 35(3), 377–391. <https://doi.org/10.5194/angeo-35-377-2017>
- Bhattacharyya, A., Beach, T. L., Basu, S., & Kintner, P. M. (2000). Nighttime equatorial ionosphere: GPS scintillations and differential carrier phase fluctuations. *Radio Science*, 35(1), 209–224. <https://doi.org/10.1029/1999RS002213>
- Boehm, J., Niell, A., Tregoning, P., & Schuh, H. (2006). Global mapping function (GMF): A new empirical mapping function based on numerical weather model data. *Geophysical Research Letters*, 33(7), L07304. <https://doi.org/10.1029/2005GL025546>
- Cherniak, I., Krankowski, A., & Zakharenkova, I. (2018). ROTI maps: A new IGS ionospheric product characterizing the ionospheric irregularities occurrence. *GPS Solutions*, 22(3), 69. <https://doi.org/10.1007/s10291-018-0730-1>
- Dugassa, T., Habarulema, J. B., & Nigussie, M. (2019). Longitudinal variability of occurrence of ionospheric irregularities over the American, African and Indian regions during geomagnetic storms. *Advances in Space Research*, 63(8), 2609–2622. <https://doi.org/10.1016/j.asr.2019.01.001>
- Fabbro, V., Jacobsen, K. S., & Rougerie, S. (2019). HAPEE, a statistical approach for ionospheric scintillation prediction in the polar region. Satellite Studies Group of URSI Commission G. Paper presented at the Beacon Satellite Symposium, Beacon.
- Fathy, A., & Ghamry, E. (2021). A two-dimensional lithospheric magnetic anomaly field model of Egypt using the measurements from Swarm satellites. *Geodesy and Geodynamics*, 12(3), 229–238. <https://doi.org/10.1016/j.geog.2021.03.004>
- Goldovsky, N., & Luria, M. (2004). Ionospheric delay contribution to the uncertainty of time and frequency measurements by one-way satellite time transfer method. *Measurement*, 35(4), 353–362. <https://doi.org/10.1016/j.measurement.2004.03.002>
- Guo, K., Vadakke Veetil, S., Weaver, B. J., & Aquino, M. (2021). Mitigating high latitude ionospheric scintillation effects on GNSS Precise Point Positioning exploiting 1-s scintillation indices. *Journal of Geodesy*, 95(3), 30. <https://doi.org/10.1007/s00190-021-01475-y>
- Jayachandran, P. T., Langley, R. B., Macdougall, J. W., Mushini, S. C., Pokhotelov, D., Hamza, A. M., et al. (2009). Canadian high arctic ionospheric network (CHAIN). *Radio Science*, 44(1), 1–10. <https://doi.org/10.1029/2008RS004046>
- Jiao, Y., & Morton, Y. T. (2015). Comparison of the effect of high-latitude and equatorial ionospheric scintillation on GPS signals during the maximum of solar cycle 24. *Radio Science*, 50(9), 886–903. <https://doi.org/10.1002/2015RS005719>
- Jiao, Y., Morton, Y. T., Taylor, S., & Pelgrum, W. (2013). Characterization of high-latitude ionospheric scintillation of GPS signals. *Radio Science*, 48(6), 698–708. <https://doi.org/10.1002/2013RS005259>
- Juan, J. M., Aragon-Angel, A., Sanz, J., González-Casado, G., & Rovira-García, A. (2017). A method for scintillation characterization using geodetic receivers operating at 1 Hz. *Journal of Geodesy*, 91(11), 1383–1397. <https://doi.org/10.1007/s00190-017-1031-0>
- Juan, J. M., Sanz, J., Rovira-García, A., González-Casado, G., Ibáñez, D., & Orus Pérez, R. (2018). AATR an ionospheric activity indicator specifically based on GNSS measurements. *Journal of Space Weather and Space Climate*, 8, A14. <https://doi.org/10.1051/swsc/2017044>
- Karatay, S. (2020). Temporal variations of the ionospheric disturbances due to the seasonal variability over Turkey using IONOLAB-FFT algorithm. *Geodesy and Geodynamics*, 11(3), 182–191. <https://doi.org/10.1016/j.geog.2019.12.002>
- Khazanov, G. V. (2016). *Space weather fundamentals* (1st ed). CRC Press.
- Lagler, K., Schindelegger, M., Böhm, J., Krásná, H., & Nilsson, T. (2013). GPT2: Empirical slant delay model for radio space geodetic techniques. *Geophysical Research Letters*, 40(6), 1069–1073. <https://doi.org/10.1002/grl.50288>
- Li, G., Ning, B., Wang, C., Abdu, M. A., Otsuka, Y., Yamamoto, M., et al. (2018). Storm-enhanced development of postsunset equatorial plasma bubbles around the meridian 120°E/60°W on 7–8 September 2017. *Journal of Geophysical Research: Space Physics*, 123(9), 7985–7998. <https://doi.org/10.1029/2018JA025871>
- Lilly, J. M., & Olhede, S. C. (2009). Wavelet ridge estimation of jointly modulated multivariate oscillations. In *2009 conference record of the forty-third asilomar conference on signals, systems and computers November 1–4 2009* (pp. 452–456).
- Linty, N., Dovis, F., & Alfonsi, L. (2018). Software-defined radio technology for GNSS scintillation analysis: Bring Antarctica to the lab. *GPS Solutions*, 22(4), 96. <https://doi.org/10.1007/s10291-018-0761-7>
- Liu, L., Su, X., & Wang, G. (2015). On inversion of continuous wavelet transform. *Open Journal of Statistics*, 5(7), 714–720. <https://doi.org/10.4236/ojs.2015.57071>
- Luan, X., Wang, W., Dou, X., Burns, A., & Yue, X. (2015). Longitudinal variations of the nighttime E layer electron density in the auroral zone. *Journal of Geophysical Research: Space Physics*, 120(1), 825–833. <https://doi.org/10.1002/2014JA020610>
- Ma, G., & Maruyama, T. (2006). A super bubble detected by dense GPS network at East Asian longitudes. *Geophysical Research Letters*, 33(21), L21103. <https://doi.org/10.1029/2006GL027512>
- Maltseva, O., & Nikitenko, T. (2021). The effect of space weather on the ionosphere at the 110° meridian during CAWSES-II period. *Geodesy and Geodynamics*, 12(2), 93–101. <https://doi.org/10.1016/j.geog.2021.03.001>
- Matzka, J., Stolle, C., Yamazaki, Y., Bronkalla, O., & Morschhauser, A. (2021). The geomagnetic Kp index and derived indices of geomagnetic activity. *Space Weather*, 19(5), e2020SW002641. <https://doi.org/10.1029/2020SW002641>
- McCaffrey, A. M., Jayachandran, P. T., Langley, R. B., & Sleewaegen, J. M. (2018). On the accuracy of the GPS L2 observable for ionospheric monitoring. *GPS Solutions*, 22(1), 23. <https://doi.org/10.1007/s10291-017-0688-4>
- Meeus, J. (1998). *Astronomical algorithms* (2nd ed). Willmann-Bell, Inc.
- Mitchell, C. N., Alfonsi, L., De Franceschi, G., Lester, M., Romano, V., & Wernik, A. W. (2005). GPS TEC and scintillation measurements from the polar ionosphere during the October 2003 storm. *Geophysical Research Letters*, 32(12). <https://doi.org/10.1029/2004GL021644>
- Moraes, A. O., Costa, E., Abdu, M. A., Rodrigues, F. S., de Paula, E. R., Oliveira, K., & Perrella, W. J. (2017). The variability of low-latitude ionospheric amplitude and phase scintillation detected by a triple-frequency GPS receiver. *Radio Science*, 52(4), 439–460. <https://doi.org/10.1002/2016RS006165>
- Nguyen, V. K., Rovira-García, A., Juan, J. M., Sanz, J., González-Casado, G., La, T. V., & Ta, T. H. (2019). Measuring phase scintillation at different frequencies with conventional GNSS receivers operating at 1 Hz. *Journal of Geodesy*, 93(10), 1985–2001. <https://doi.org/10.1007/s00190-019-01297-z>
- Oksavik, K., van der Meeren, C., Lorentzen, D. A., Baddeley, L. J., & Moen, J. (2015). Scintillation and loss of signal lock from poleward moving auroral forms in the cusp ionosphere. *Journal of Geophysical Research: Space Physics*, 120(10), 9161–9175. <https://doi.org/10.1002/2015JA021528>
- Olhede, S. C., & Walden, A. T. (2002). Generalized Morse wavelets. *IEEE Transactions on Signal Processing*, 50(11), 2661–2670. <https://doi.org/10.1109/TSP.2002.804066>
- Pi, X., Mannucci, A. J., Lindqwister, U. J., & Ho, C. M. (1997). Monitoring of global ionospheric irregularities using the Worldwide GPS Network. *Geophysical Research Letters*, 24(18), 2283–2286. <https://doi.org/10.1029/97GL02273>

- Prikryl, P., Ghoddousi-Fard, R., Weygand, J. M., Viljanen, A., Connors, M., Danskin, D. W., et al. (2016). GPS phase scintillation at high latitudes during the geomagnetic storm of 17–18 March 2015. *Journal of Geophysical Research: Space Physics*, *121*(10), 10448–10465. <https://doi.org/10.1002/2016JA023171>
- Torrence, C., & Compo, G. P. (1998). A practical guide to wavelet analysis. *Bulletin of the American Meteorological Society*, *79*(1), 61–78. [https://doi.org/10.1175/1520-0477\(1998\)079<0061:APGTWA>2.0.CO;2](https://doi.org/10.1175/1520-0477(1998)079<0061:APGTWA>2.0.CO;2)
- Van Dierendonck, A. J., Klobuchar, J., & Hua, Q. (1993). *Ionospheric scintillation monitoring using commercial single frequency C/A code receivers*. Institute of Navigation. Paper presented at ION GPS 1993.
- Vani, B. C., Shimabukuro, M. H., & Galera Monico, J. F. (2017). Visual exploration and analysis of ionospheric scintillation monitoring data: The ISMR Query Tool. *Computers & Geosciences*, *104*, 125–134. <https://doi.org/10.1016/j.cageo.2016.08.022>
- Wu, J. T., Wu, S. C., Hajj, G. A., Bertiger, W. I., & Lichten, S. M. (1992). Effects of antenna orientation on GPS carrier phase. *Astrodynamics*, 1647–1660.
- Xu, F., Li, Z., Zhang, K., Wang, N., Wu, S., Hu, A., et al. (2020). An investigation of optimal machine learning methods for the prediction of ROTI. *Journal of Geodesy and Geoinformation Science*, *3*(2), 1–15. <https://doi.org/10.11947/j.JGGS.2020.0201>
- Yang, Z., & Liu, Z. (2016). Correlation between ROTI and ionospheric scintillation indices using Hong Kong low-latitude GPS data. *GPS Solutions*, *20*(4), 815–824. <https://doi.org/10.1007/s10291-015-0492-y>
- Yizengaw, E., & Groves, K. M. (2018). Longitudinal and seasonal variability of equatorial ionospheric irregularities and electrodynamics. *Space Weather*, *16*(8), 946–968. <https://doi.org/10.1029/2018SW001980>
- Zhao, D., Hancock, C. M., Roberts, G. W., & Jin, S. (2019). Cycle slip detection during high ionospheric activities based on combined triple-frequency GNSS signals. *Remote Sensing*, *11*(3), 250. <https://doi.org/10.3390/rs11030250>
- Zhao, D., Li, W., Li, C., Hancock, C. M., Roberts, G. W., & Wang, Q. (2022). Analysis on the ionospheric scintillation monitoring performance of ROTI extracted from GNSS observations in high-latitude regions. *Advances in Space Research*, *69*(1), 142–158. <https://doi.org/10.1016/j.asr.2021.09.026>
- Zhao, D., Li, W., Wang, Q., Liu, X., Li, C., Hancock, C. M., et al. (2022). Statistical study on the characterization of phase and amplitude scintillation events in the high-latitude region during 2014–2020 based on ISMR. *Advances in Space Research*, *69*(9), 3435–3459. <https://doi.org/10.1016/j.asr.2022.02.031>
- Zhao, D., Roberts, G. W., Hancock, C. M., Lau, L., & Bai, R. (2019). A triple-frequency cycle slip detection and correction method based on modified HMW combinations applied on GPS and BDS. *GPS Solutions*, *23*(1), 22. <https://doi.org/10.1007/s10291-018-0817-8>